ADVANCED FUNCTIONAL MATERIALS
www.afm-journal.de

Powering the Future: A Cobalt-Based Catalyst for Longer-Lasting Zinc–Air Batteries

Manami Banerjee, Peng Ren, Greesh Kumar, Lucie Lindenbeck, Byoung Joon Park, Anna Rokicińska, Piotr Kuśtrowski, Adam Slabon, Francesco Ciucci, Ramendra Sundar Dey, and Shoubhik Das**

The development of cost-effective catalysts for zinc–air batteries (ZABs) remain challenging due to the sluggish kinetics of oxygen reduction (ORR) and evolution (OER) at the cathode. In this context, a novel N-doped graphitic shell-encapsulated cobalt catalyst is presented as an air electrode with exceptional bifunctional activity, achieving an ORR half-wave potential ($E_{1/2}$) of 0.81 V and an OER overpotential of 349 mV in an alkaline medium. The catalyst demonstrated excellent cycling durability and delivered superior power density in both liquid and solid-state ZABs. Furthermore, a quasi-solid-state ZAB is assembled with the catalyst, and it maintained a stable open-circuit voltage (OCV) of 1.360 V for >10 000 s. The catalyst achieved a peak power density of 127 mW cm^{-2}—significantly outperforming the benchmark Pt/C + RuO_2 system (74 mW cm^{-2}). When two tandem-junction ZABs are connected in series, they achieved an OCV of 2.75 V and powering a "ZAB" LED strip and a mini fan. Furthermore, Density Functional Theory (DFT) calculations revealed that the enhanced performance resulted from optimized binding energies between the Co@N(py) active sites and reaction intermediates. An in situ Raman study is carried out to understand the catalytic mechanism through transient intermediate detection.

1. Introduction

The escalating energy demands of modern society have driven significant efforts toward the development of sustainable energy technologies.[1] Batteries play a key role in this transition by enabling efficient energy storage and its delivery, bridging the gap between energy production and consumption.[2] In this regard, lithium-ion batteries (LIBs) and supercapacitors (SCs) have emerged as advantageous energy storage technologies owing to their elevated energy and power densities, rechargeability, and efficiency, rendering them ideal for powering electronic devices and facilitating the integration of renewable energy sources.[3] However, despite their widespread adoption, LIBs and SCs face significant limitations, including relatively low intrinsic energy density, environmental concerns related to resource extraction, recycling, and the constrained availability of critical raw materials such as lithium.[4] These challenges have driven researchers to explore alternative systems that are more sustainable and economically viable. Given these constraints, zinc–air batteries (ZABs) present a viable alternative for next-generation energy storage devices.[4] Particularly, ZABs employ zinc, an abundant element, at the negative electrode and oxygen as the positive electrode reactant, offering a cost-effective and environmentally friendly alternative with a theoretical energy density of 1084 Wh kg^{-1}

M. Banerjee, P. Ren, S. Das
Department of Chemistry
University of Bayreuth
Universitätsstraße 30, 95447 Bayreuth, Germany
E-mail: Shoubhik.Das@uni-bayreuth.de

G. Kumar, R. S. Dey
Institute of Nano Science and Technology (INST)
Sector-81, Mohali, Punjab 140306, India
E-mail: rsdey@inst.ac.in

The ORCID identification number(s) for the author(s) of this article can be found under https://doi.org/10.1002/adfm.202519329

DOI: 10.1002/adfm.202519329

L. Lindenbeck, A. Slabon
Chair of Inorganic Chemistry
University of Wuppertal
Gaußstraße 20, 42119 Wuppertal, Germany

B. J. Park, F. Ciucci
Chair of Electrode Design for Electrochemical Energy Systems
University of Bayreuth
Weiherstraße 26, 95448 Bayreuth, Bavaria, Germany

B. J. Park, F. Ciucci
Bavarian Center for Battery Technology (BayBatt)
University of Bayreuth
Universitätsstraße 30, 95447 Bayreuth, Germany

A. Rokicińska, P. Kuśtrowski
Faculty of Chemistry
Jagiellonian University
Gronostajowa 2, Kraków 30–387, Poland

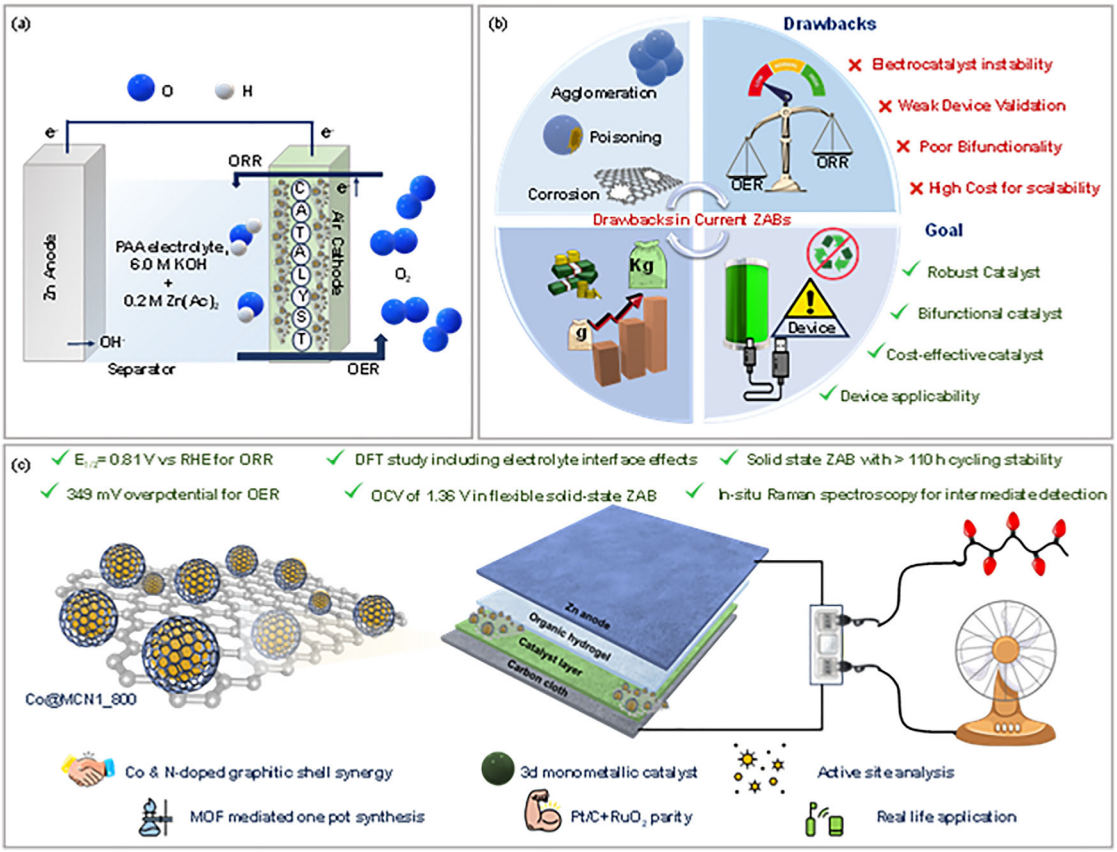

Figure 1. a) Working principle of a Liquid ZAB system; b) Drawbacks in current ZAB strategies; c) Our work.

(≈3 to 4 times that of traditional lithium-ion batteries).[4,5] Moreover, ZABs offer extensive safety due to their non-flammable aqueous electrolytes, and feature optimal design flexibility for both primary and rechargeable configurations, making them highly attractive for large-scale grid storage as well as portable applications.[6]

Despite their appealing features, the commercial viability of ZABs is hindered by critical challenges, particularly the sluggish kinetics of the oxygen reduction reaction (ORR) and oxygen evolution reaction (OER), which are essential for their efficient rechargeable operation (**Figure 1a**).[7–11] In ZABs, ORR occurs at the air cathode during discharge by reducing atmospheric oxygen, while OER during charging releases oxygen gas, both of which are integral to the overall electrochemical operation of the cell.[9,10] To mitigate the sluggish kinetics of ORR and OER in ZABs, noble metal-based catalysts, including Pt, Ru, and Ir, have been extensively investigated.[12–14] Nevertheless, the limited availability and high cost of noble-metal-based catalysts elevate the overall expense of the process and often suffer from degradation of activity over prolonged cycling, compromising the long-term reliability of the batteries.[15] Additionally, their restricted bifunctional activity does not satisfy the criteria for effective and reversible oxygen electrocatalysis (Figure 1b).[5,16] These concerns have prompted the research community to explore stable and cost-effective alternatives for ZAB. In this regard, first-row transition metal-doped carbon materials have gained substantial attention, attributed to their economic viability, superior catalytic efficiency, and robust stability across a wide range of various catalytic applications.[17–21]

Recently, porous organic frameworks, carbon-based materials such as carbon nanotubes, graphene, and nitrogen-doped carbon have garnered interest as ORR and OER electrocatalysts due to their superior conductivity and durability.[22–26] Specifically, when combined with 3d transition metal (M) nanoparticles (NPs = Co, Fe, Ni, Mn), these composites exhibit enhanced ORR/OER activity, attributed to improved charge transfer kinetics and a profusion of active sites.[27–29] In particular, Co has obtained specific attention due to its variable oxidation states (Co^{II}/Co^{III}), and closely aligned redox potential compared to the potential of O_2 reduction to water ($E = 1.23$ V vs Reversible Hydrogen electrode or RHE).[30,31] However, their long-term stability remains a key concern, as metal NPs may leach from the carbon matrix under high overpotentials and prolonged cycling, leading to corrosion, passivation, and active site degradation.[32–39] To overcome these limitations, Metal Organic framework (MOF)-derived carbon-encapsulated metal hybrids with well-defined 3D architectures have emerged as a promising solution, offering improved structural confinement and enhanced durability.[40] The carbon shell facilitates electron transmission and safeguards metal cores from oxidation, while nitrogen doping from MOF precursors creates active $M–N_x$ sites for the ORR and OER.[41–46] Inspired by this, we report a MOF-mediated confined pyrolysis strategy to synthesize

a monometallic bifunctional catalyst which features Co-NPs encapsulated in *N*-doped graphitic shells on a carbon matrix. This design enhances conductivity and tunes the electronic structure of ORR/OER active sites. At the same time, the synergistic interaction between Co and the carbon shell improves metal–support interaction and prevents agglomeration, leaching, and corrosion. In fact, an outstanding ORR performance, with ($E_{1/2}$) of 0.81 V versus RHE and a limiting current density of 5.3 mA cm^{-2}, comparable to commercial Pt/C (0.83 V, 4.6 mA cm^{-2}) was observed along with a low OER overpotential of 349 mV, very comparable to that of RuO_2 (322 mV) (Figure 1c)! Intrigued by this performance, when employed in a quasi-solid-state ZABs, the catalyst delivered a stable open-circuit voltage (OCV) of 1.360 V for >10 000 s and a peak power density of 127 mW cm^{-2}, significantly surpassing the benchmark Pt/C + RuO_2 system (74 mW cm^{-2}). Building on this performance, two tandem-junction ZABs were connected in series, achieving an OCV of 2.75 V and powering a "ZAB" LED strip. Notably, the setup maintained a stable red LED (≈2.75 V) for 6 h with minimal voltage drop. Furthermore, the computational study at the DFT level including projected density of states (PDOS) analyses revealed that our Co-based catalyst consisted of Co@N(py) active sites which exhibited lower adsorption energies for ORR and OER intermediates. Additionally, the electron redistribution at the Co@N(py) interface suggested a synergistic effect among Co centers (enhances intermediates adsorption) and pyridinic coordination environment of the N-doped carbon layer (which influences catalytic activity), providing fundamental insights into its superior bifunctional electrocatalytic activity. The mechanistic study done by using in situ Raman spectroscopic for determination of the intermediates involved during the ORR and OER electrocatalysis in alkaline media.

2. Results and Discussion

2.1. Synthesis and Characterization

2.1.1. General Synthesis

Co@MCN1 (before pyrolysis) and Co@MCN1_800 (after pyrolysis) were prepared by following a two-step solvothermal-pyrolysis process (please see detailed procedure in the S1.2.1, Supporting Information). The catalyst is referred as Co@MCN1, where "Co" represents cobalt as the active metal doped within N-doped carbon matrix (MCN1). In both cases, $Co(NO_3)_2.6H_2O$ was taken as a cobalt precursor while 1,4-diazabicyclo[2.2.2]octane (DABCO) and terephthalic acid (TPA) were used as organic linkers (**Figure** 2a). Initially, cobalt ions were coordinated with DABCO and TPA in DMF to form a Co-MOF precursor at 150 °C. Afterward, Vulcan XC72R carbon was introduced as a support, and the mixture was refluxed and subsequently heated to ≈180 °C to induce slow solvent evaporation, which facilitated the in situ growth of Co-MOF on the carbon surface. The resulting composite was dried, ground, and labelled as Co@MCN1 (non-pyrolyzed). A portion of this material was then subjected to pyrolysis under N_2 atmosphere at 800 °C to yield Co@MCN1_800 (pyrolyzed) which consisted of well-dispersed Co-nanoparticles confined within *N*-doped graphitic layers.

2.1.2. Powder X-Ray Diffraction (XRD)

The powder XRD patterns of Co@MCN1 and Co@MCN1_800 revealed distinct structural differences (Figure 2b). Co@MCN1 displayed mainly broad reflection peaks, indicative of its predominantly bad crystallinity the absence of metallic crystalline cobalt. In contrast, Co@MCN1_800 exhibited a prominent reflection peak at $2\theta \approx 26°$, corresponding to the (002) plane of graphitic carbon, confirming graphitization upon thermal treatment. The broad reflection peaks at $2\theta \approx 45°$ and 52° can be indexed with the (111) and (200) planes of face-centered cubic (fcc) cobalt, respectively, confirming thus the formation of crystalline metallic Co. The emergence of these reflection peaks after pyrolysis confirmed the formation of crystalline graphitic carbon and the successful reduction of cobalt species, validating the structural evolution from the MOF precursor (Co@MCN1) to the active catalyst phase (Co@MCN1_800).

2.1.3. Transmission Electron Microscopy (TEM)

The morphological structure of Co@MCN1_800 was investigated using TEM (Figure 2c). The catalyst consisted of dispersed Co nanoparticles (high-contrast dark features are visible in the image), embedded within a carbonaceous matrix, confirming the effective integration of active sites. Furthermore, TEM analyses of the electrocatalyst and post-catalysis revealed an analogous morphology, thereby suggesting that the structural integrity of the catalyst was retained under the catalytic conditions (Figures S2–S5, Supporting Information).

2.1.4. X-Ray Absorption Spectroscopy (XAS)

X-ray absorption spectroscopy (XAS) was also utilized to examine the local environment and electronic properties of cobalt-based catalysts during their preparation and utilization (Figure 2d). It should be noted that all *R*-space spectra were shown to have an uncorrected phase shift, meaning that the actual interatomic distances were slightly longer than the apparent *R* values. The *R*-space spectrum of Co@MCN1, prior to pyrolysis, exhibited low-intensity Co-Co peaks, which suggested a low metallic content in the material. Furthermore, a higher intensity signal at ≈ 1.54 Å in this material demonstrated the Co-N interactions between the N atom of DABCO and Co^{2+}. On the other hand, after the pyrolysis process (Co@MCN1_800), the XAS data revealed the presence of a primary Co-Co shell (Figure 2e,f). A thorough examination of the data indicated a coordination number of 12 for Co in Co@MCN1_800 and a Co—Co bond length of 2.49 Å.

These findings served to substantiate the existence of a well-ordered metallic Co phase. In this aspect, post-catalysis of Co@MCN1_800 exhibited a similar XAS spectrum, retaining the similar bond length and coordination number (Figure S6 and Table S1, Supporting Information). This was aligned with the result from TEM and further supported the structural stability of our catalyst under reaction conditions.

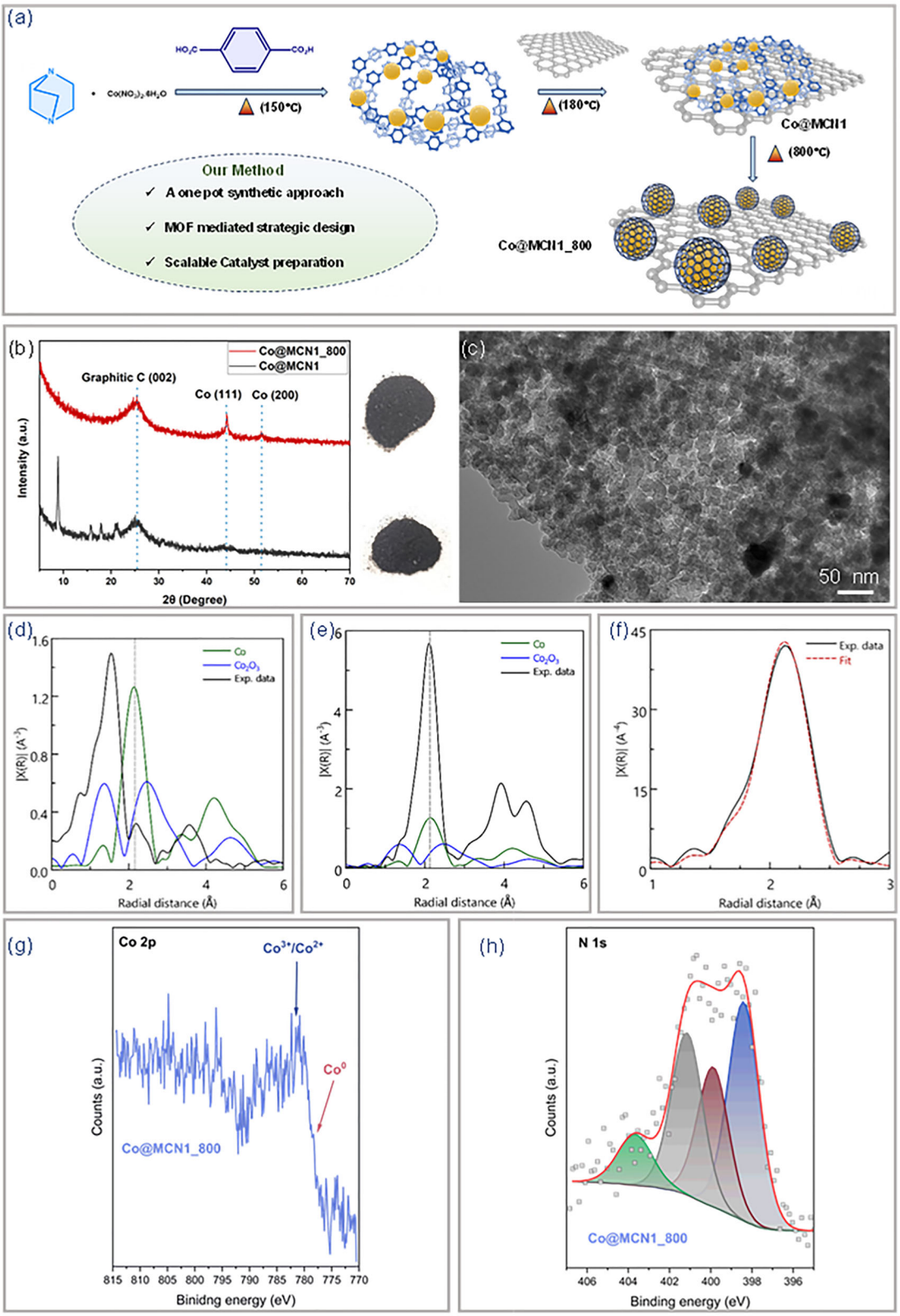

Figure 2. a) Synthesis procedure of the catalyst; b) Powder XRD patterns of Co@MCN1 and Co@MCN1_800 and the images of the catalysts before grinding; c) TEM image of Co@MCN1_800 before catalysis; d) Fourier transform (FT) of the Co K-edge XAS spectra of Co@MCN1, Co powder and Co_2O_3; e) Fourier transform (FT) of the Co K-edge XAS spectra of Co@MCN1_800, Co powder and Co_2O_3; f) corresponding fitting curve in the 1.0 Å < R < 3 Å interval (right); g) Co 2p XPS spectrum for Co@MCN1_800; h) N 1s XPS spectrum for Co@MCN1_800.

2.1.5. X-Ray Photoelectron Spectroscopy (XPS)

The surface composition of the Co@MCN1_800 was further investigated by using XPS. The measurements were performed on four different surface regions to confirm the uniformity of the component distribution, and Figure 2g,h presents the averaged Co 2p and N 1s spectra for these surface areas, respectively. It was observed that the surface was predominantly composed of carbon (> 95 at.%). Additionally, nitrogen was incorporated into the carbon matrix, with the atomic N/C ratio of 0.023 ± 0.004. In fact, three main forms – pyridinic, pyrrolic, and quaternary N – were confirmed by the presence of N 1s peaks which were located at 398.4 , 400.2 , and 401.0 eV, respectively.[47] However, an additional N 1s component was observed at higher binding energy (403.5 eV) which could be attributed to oxidized N species in Co@MCN1_800. Furthermore, small quantity of cobalt (0.23 ± 0.03 at.%) was also detected on the surface. On the other hand, in the Co $2p_{3/2}$ region, a distinct photoelectron emission was observed at binding energies of 780–782 eV along with additional features at ≈ 778.5 eV. The first peak corresponded to the oxidized Co species, i.e., Co^{2+} and/or Co^{3+}, while the latter was attributed to metallic cobalt (Co^0).[48] In addition to this, a rough estimation suggested that, in the case of fresh Co@MCN1_800, the ratio of metallic to oxidized Co was ca. 1:4. For the sample after catalysis, the distribution of Co species was largely preserved (Figure S7, Supporting Information), with the contribution of metallic Co decreasing only slightly to ca. 1:6 (Table S2, Supporting Information), which confirms the good anti-corrosion efficacy of the carbon shell.[47,48]

2.1.6. Raman Spectroscopy

To understand the different extent of graphitization in Co@MCN1_800 and Co@MCN1 we performed Raman spectroscopy. Raman spectra exhibited characteristic D band about at 1345 cm^{-1} and a G band at 1683 cm^{-1} for both materials (Figure S8, Supporting Information). The D and G peaks in Co@MCN1_800 are attributed to the disordered aromatic structure of sp^3 bonded carbon, and the bond stretching of sp^2 atoms of typical graphite, respectively.[49] The intensity ratio of the D band to the G band (I_D/I_G) provides a semi-quantitative assessment of graphitization degree and often referred as a defect and graphitization indicator, consistent with the scientific literature. The lower I_D/I_G ratio indicates fewer defects and a higher degree of graphitization. Specifically, Co@MCN1_800 shows an I_D/I_G ratio of 0.96, lower than the value of 1.09 for Co@MCN1. This decrease in the I_D/I_G ratio suggests that the pyrolysis step introduces greater graphitization into the carbon framework.

2.2. Optimization in Oxygen Reduction Reaction (ORR) as Well as in Oxygen Evolution Reaction (OER)

2.2.1. ORR

The ORR performance was evaluated by using the rotating disk electrode (RDE) & rotating ring disk electrode (RRDE) technique in an O_2-saturated 0.1 M KOH solution. Furthermore, the results were compared with the commercially available Pt/C (20 wt%) catalyst, which is known to be a highly active catalyst in ORR. At first, the cyclic voltammetry (CV) response was recorded for Co@MCN1_800 in an argon as well as O_2-saturated alkaline solution at a scan rate of 0.1 V s^{-1} (Figure S9, Supporting Information). To our observation, a rectangular shape curve was obtained in Ar-saturated solution, while a sharp cathodic reduction peak was observed in an O_2-saturated solution, confirming the ORR activity of Co@MCN1_800. The linear sweep voltammetry (LSV) was also carried out using RRDE electrodes and compared with commercially available Pt/C at 1600 rpm with a potential of 5 mV s^{-1} scan rate (**Figure 3a**). To our surprise, Co@MCN1_800 exhibited a half-wave ($E_{1/2}$) potential of 0.81 V versus RHE and a limiting current density (J_L) of 5.3 mA cm^{-2}, which is quite comparable to that of 20 wt.% Pt/C catalyst ($E_{1/2}$ = 0.83 V, J_L 4.6 mA cm^{-2}; Table S3, Supporting Information). In contrast, a significant drop in activity was observed when Co@MCN1 was tested under similar conditions, delivering only 2.9 mA cm^{-2} of current density and a $E_{1/2}$ of 0.75 V.

Motivated by these observations, we were intrigued to understand the superior activity of the Co@MCN1_800 compared to its non-pyrolyzed counterpart (Co@MCN1). We further investigated the reaction kinetics by analyzing the Tafel slope, derived from LSV measurements conducted at a scan rate of 5 mV s^{-1} at 1600 rpm. The Tafel slope indicates how rapidly the overpotential increases with current density during an electrochemical reaction; a lower Tafel slope signifies faster electron transfer and enhanced catalytic activity. Indeed, the faster electrochemical kinetics of the Co@MCN1_800 was confirmed from the Tafel slope (65 mV dec^{-1}) compared to Co@MCN1 (77 mV dec^{-1}) and even commercially available Pt/C catalyst (77 mV dec^{-1}) (Figure 3b). To investigate whether this improvement stemmed from increased electro-chemically active surface area (ECSA) or not, cyclic voltammetry (CV) was also conducted in the non-Faradaic region at scan rates ranging from 30 to 100 mV s^{-1} for both Co@MCN1 and Co@MCN1_800 (Figures S10 and S11, Supporting Information). Furthermore, the double layer capacitance (C_{dl}) plot was achieved from the slope of the current versus scan rate plot, where the linear fit provided an electrochemically active surface area (ECSA) of 0.303 cm^2 for Co@MCN1 and 0.338 cm^2 for Co@MCN1_800, respectively. Given the negligible difference in ECSA, the enhanced ORR activity of Co@MCN1_800 can be primarily attributed to its improved intrinsic reaction kinetics.

To understand the kinetic and mass transfer limitation in Co@MCN1_800, linear sweep voltammetry (LSV) was recorded at different rotation speeds ranging from 400 to 2400 rpm (Figure S12, Supporting Information). In general, increasing the rotation rate enhances oxygen supply to the electrode surface, thereby reducing both kinetic and mass transport limitations. This results in improved current response, demonstrating that higher rotation speed promote faster and more efficient oxygen reduction. Accordingly, the LSV curves of Co@MCN1_800 at different rotations exhibited enhancement in current density along with the increasing rate of rotations (rpm), which further confirmed that with the enhanced O_2 availability, mass transport was facilitated by Co@MCN1_800 (superior ORR activity under diffusion-controlled regions). To further explore the catalytic mechanism, Koutecky–Levich (K-L) equation with the LSV curves recorded

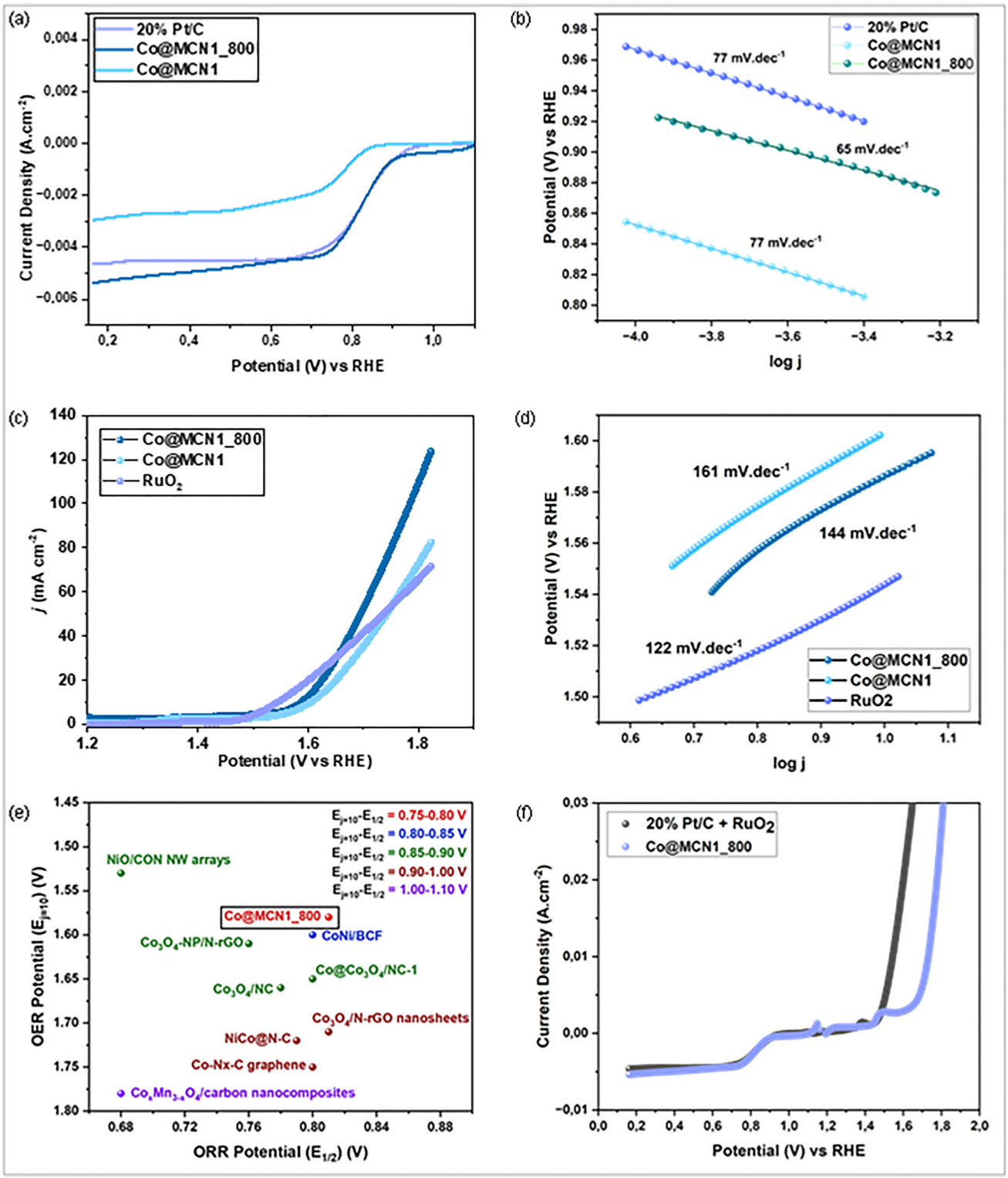

Figure 3. a) LSV curves for ORR in 0.1 M KOH; b) Tafel plot for the respective catalysts under scanning rate 5 mV s^{-1} for ORR; c) LSV curves for OER activity in 1 M KOH d) Tafel plot for the respective catalysts under scanning rate 1 mV s^{-1} for OER; e) Previous literature and our work f) Comparison of overall bifunctional activity of Co@MCN1_800 and Pt/C+RuO_2.

Table 1. Catalyst comparison table.

Catalyst	OER $E_{j=10}$ [V]	ORR $E_{1/2}$ [V]	ΔE [V] = $E_{j=10} - E_{1/2}$	Refs.
Co@MCN1_800	**1.58**	**0.81**	**0.77**	**This work**
NiCo@N-C	1.71	0.81	0.9	[52]
Co@Co_3O_4/NC-1	1.65	0.8	0.85	[53]
Co_3O_4/N-rGO nanosheets	1.72	0.79	0.93	[54]
Co_3O_4-NP/N-RGO	1.61	0.76	0.85	[55]
Co-Nx-C graphene	1.75	0.8	0.95	[56]
NiO/CoN NW arrays	1.53	0.68	0.85	[57]
CoNi/BCF	1.6	0.8	0.8	[58]
Co_3O_4/NC	1.66	0.78	0.88	[59]
$Co_xMn_{3-x}O_4$ carbon nanocomposites	1.78	0.68	1.1	[60]

on various rotation speeds (400 to 2400 rpm) at various applied potentials (0.72 to 0.52 V). The linear relationship between the inverse current density (1/J) and the inverse square root of the rotation speed ($\omega^{-1/2}$) at various applied potentials referring to the K-L plot indicated that the ORR on Co@MCN1_800 followed first-order reaction kinetics with respect to the dissolved oxygen concentration (Figure S12, Supporting Information). Furthermore, the nonzero K–L intercept suggested that side reactions might be occurring during ORR, possibly due to intermediate species spreading onto nearby surfaces – a phenomenon termed as "spillover".[50,51] The K-L and Ring-current density (Figure S13, Supporting Information) measurement revealed an average electron transfer of ≈ 3.6 per O_2 molecule across the potential range of 0.72–0.52 V (vs RHE). This indicates a near four-electron pathway and further confirmed the first-order ORR kinetics for Co@MCN1_800 where O_2 was converted to OH^- and rather than HO_2^-. This is particularly advantageous for Co@MCN1_800 since this facilitated to bypass the formation of peroxide species to avoid the degradation of membrane in fuel cells.

Furthermore, the stability of the Co@MCN1_800 was evaluated by chronoamperometric analysis, and the relative current remained 93% even after 20 h! This clearly indicated the robust nature and sustained catalytic efficiency during prolonged operation (Figure S14, Supporting Information). Additionally, the methanol tolerance measurement was conducted by using *i-t* chronoamperometry response and CV technique with the addition of 2 mL CH_3OH (Figure S15, Supporting Information) to understand the applicability of our catalyst in a methanol fuel cell. To our delight, the current density of Co@MCN1_800 recovered rapidly after transitory disturbance and that clearly indicated the methanol resistance ability of Co@MCN1_800, making it a promising candidate for direct methanol fuel cell applications.

2.2.2. OER

To explore the suitability of our catalyst for the ZAB system, we were intrigued to investigate the bifunctionality of our catalyst in OER. For this purpose, we systematically evaluated Co@MCN1 and Co@MCN1_800 in the presence of 1.0 M KOH at 5 mV s^{-1}. Furthermore, we compared their performance with the state-of-the-art catalyst for OER, RuO_2. To our delight, both Co@MCN1 and Co@MCN1_800 demonstrated an excellent activity, requiring 369 and 349 mV overpotential to achieve 10 mA.cm^{-2} current density, respectively (Figure 3c) which was comparable to RuO_2 (322 mV). Further to understand the kinetics, we investigated the Tafel slope for both catalysts. Delightfully, Co@MCN1_800 (Tafel slope: 144 mV dec^{-1}) exhibited comparable kinetics with RuO_2 (122 mV dec^{-1}) and outperformed Co@MCN1 (161 mV dec^{-1}) (Figure 3d) in terms of OER kinetics. This established that Co@MCN1_800 exerted a robust bifunctionality (Figure 3e) and should be applied in the ZAB system, considering its superior bifunctional character in ORR as well as in the OER process (Figure 3f). The table below is a comparative analysis among our catalyst and reported catalysts in the literature (a broader analysis available in Tables S4 and S5, Supporting Information) (**Table 1**).

2.3. Application in Zinc-Air Battery (ZAB)

2.3.1. Liquid State ZAB

Encouraged by the excellent bifunctional activity of Co@MCN1_800 in both ORR and OER, it was directly applied as an air cathode and was assembled into rechargeable aqueous Zn-air battery (ZAB, **Figure 4a**). The rechargeable aqueous ZAB was assembled with Co@MCN1_800 as an air cathode, a combination of electrolytes (6.0 (M) KOH along with 0.2 (M) $Zn(CH_3COO)_2$), and Zn foil (0.25 mm thickness) as the anode (Figure 4a). For comparison, a benchmark ZAB was also constructed using a 1:1 mixture of commercial Pt/C and RuO_2 as the air cathode in aqueous ZABs. Notably, the battery with Co@MCN1_800 displayed a higher open circuit voltage (OCV) of 1.42 V surpassing that of the Pt/C-RuO_2 based aqueous ZAB (1.40 V, Figure 4b). In fact, a higher OCV in Co@MCN1_800 indicated greater stored potential energy in the battery when it's not in use. Furthermore, their discharging polarization curves, and corresponding power density polarization curves, and corresponding power densities achieved a maximum power density of 188 mW cm^{-2} by aqueous ZAB with Co@MCN1_800 at 298 mA cm^{-2}, which was significantly higher than that of the benchmark-based ZAB (102 mW cm^{-2} at 124 mA cm^{-2}), exhibiting a superior discharging performance (Figure 4c).

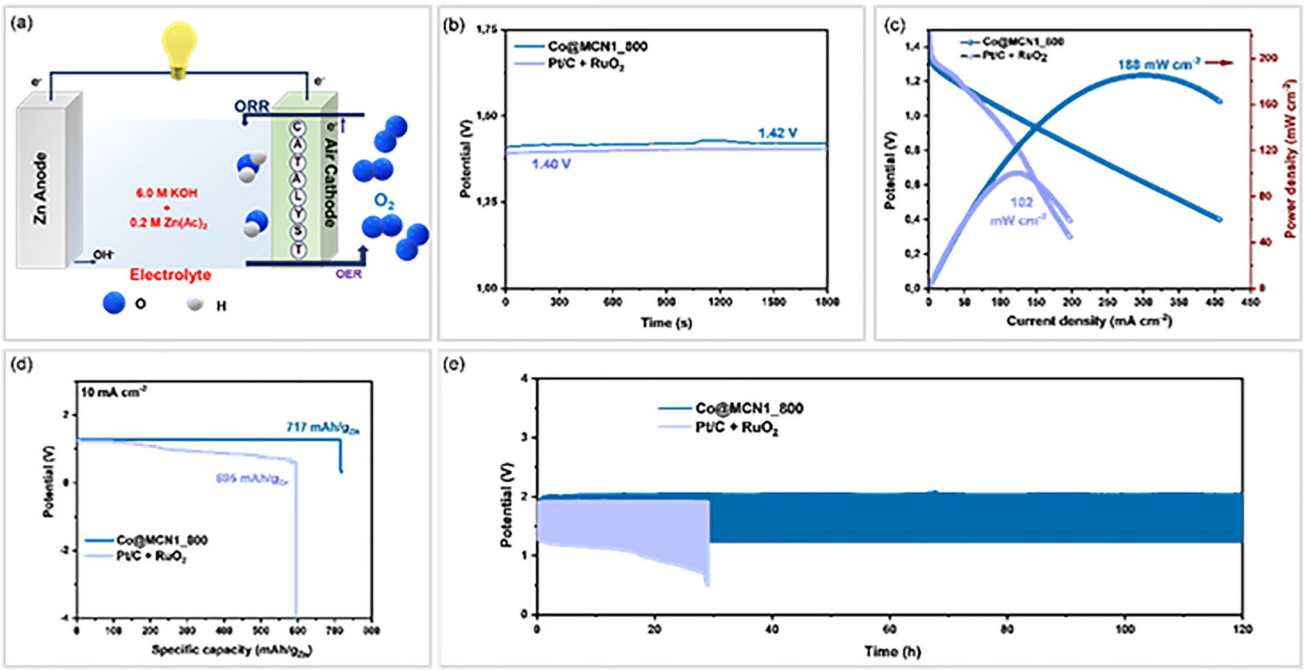

Figure 4. Electrochemical performances of liquid state Zinc-Air battery: a) Schematic presentation of liquid cell setup for ZAB; b) OCV plot of Co@MCN1_800 and (Pt/C +RuO_2) catalysts in 6.0 (M) KOH + $Zn(ac)_2.2H_2O$ electrolyte solution for liquid ZAB; c) Polarization curves and corresponding areal power plots of the Co@MCN1_800 and commercial (Pt/C+RuO_2) catalysts; d) Specific capacities of Co@MCN1_800 and (Pt/C +RuO_2) catalysts; e) Galvanostatic cycling stabilities of the liquid ZAB based on Co@MCN1_800 and (Pt/C +RuO_2) catalysts at 5 mA cm^{-2} after 5 min of charge and 5 min of discharge.

Additionally, Co@MCN1_800 had a higher specific capacity of 717 mAh/g_{Zn} at 10 mA cm^{-2} than that of the benchmark-based Pt/C-RuO_2 (695 mAh/g_{Zn}, Figure 4d). It should be noted that charging/discharging cycling stability is a crucial evaluation for a rechargeable ZAB. In this aspect, the cycling curves recorded at a constant current density of 5 mA cm^{-2} and the voltage gap of aqueous ZAB with Co@MCN1_800 exhibited negligible change during the charging–discharging cycling stability test, increasing from 0.79 to 0.83 V (Figure 4e). However, the benchmark-based ZAB showed an increasing voltage gap and degraded significantly after 20 h of stability test. These results also suggested the better stability and activity of Co@MCN1_800 than Pt/C + RuO_2 benchmark catalysts. The excellent stability of the aqueous ZAB with Co@MCN1_800 encouraged us to apply it to different electronic devices.

2.3.2. Flexible Solid-State ZAB

In addition to aqueous ZAB systems, a flexible quasi-solid-state rechargeable zinc–air battery was developed by using Co@MCN1_800 as the air cathode, polyacrylamide (PAA) hydrogel as the electrolyte, and zinc foil as the anode to develop a portable and wearable energy storage device (**Figure 5**a–c). Remarkably, the quasi-solid ZAB with Co@MCN1_800 had a stable Open-circuit voltage (OCV) stability measurements up to 1800 min (Figure 5b). These extended evaluations demonstrate sustained OCV retention and stable cycling performance. Furthermore, the discharging polarization curves of as synthesized Co@MCN1_800 and Pt/C + RuO_2 catalysts achieved a peak power density of 127 mW cm^{-2}, outperforming the Pt/C + RuO_2-based counterpart, which delivered only 74 mW cm^{-2} (Figure 5c). The voltage platform for quasi-solid-state rechargeable ZAB with Co@MCN1_800 changed slightly at different current densities (Figure 5d). In addition, the solid ZAB with Co@MCN1_800 also exhibited an excellent cycling stability of 110 h with minimum potential change (Figure 5d). This highlights the critical role of an efficient solid electrolyte in achieving a long lifespan of flexible solid-state rechargeable ZAB. Furthermore, the charge–discharge (20 min per cycle) profiles of the flexible zinc–air batteries operated at a constant current density of 2 mA cm^{-2} under various bending angles upto 1000 min (see inset Figure 5f). The consistent electrochemical performance across these mechanical deformations highlighted the excellent flexibility and structural integrity of the flexible ZAB battery. Notably, the Co@MCN1_800 electrode maintained stable charge–discharge behavior throughout the bending cycles. This mechanical robustness is particularly important for powering next-generation portable and wearable electronics, where adaptability to dynamic shapes and motions is essential without compromising energy output or cycling stability. Furthermore, a mini fan was powered by the flexible ZAB with Co@MCN1_800 and ran smoothly as demonstrated (Figure 5g). Delighted by this, further potential of the flexible solid ZABs was demonstrated by connecting two batteries in series for practical application. In fact, the tandem-junction ZABs exhibited an OCV of 2.75 V and easily lightened a "ZAB" LED strip (Figure 5h). After demonstrating practical applicability, two ZABs were successfully connected in series to power a

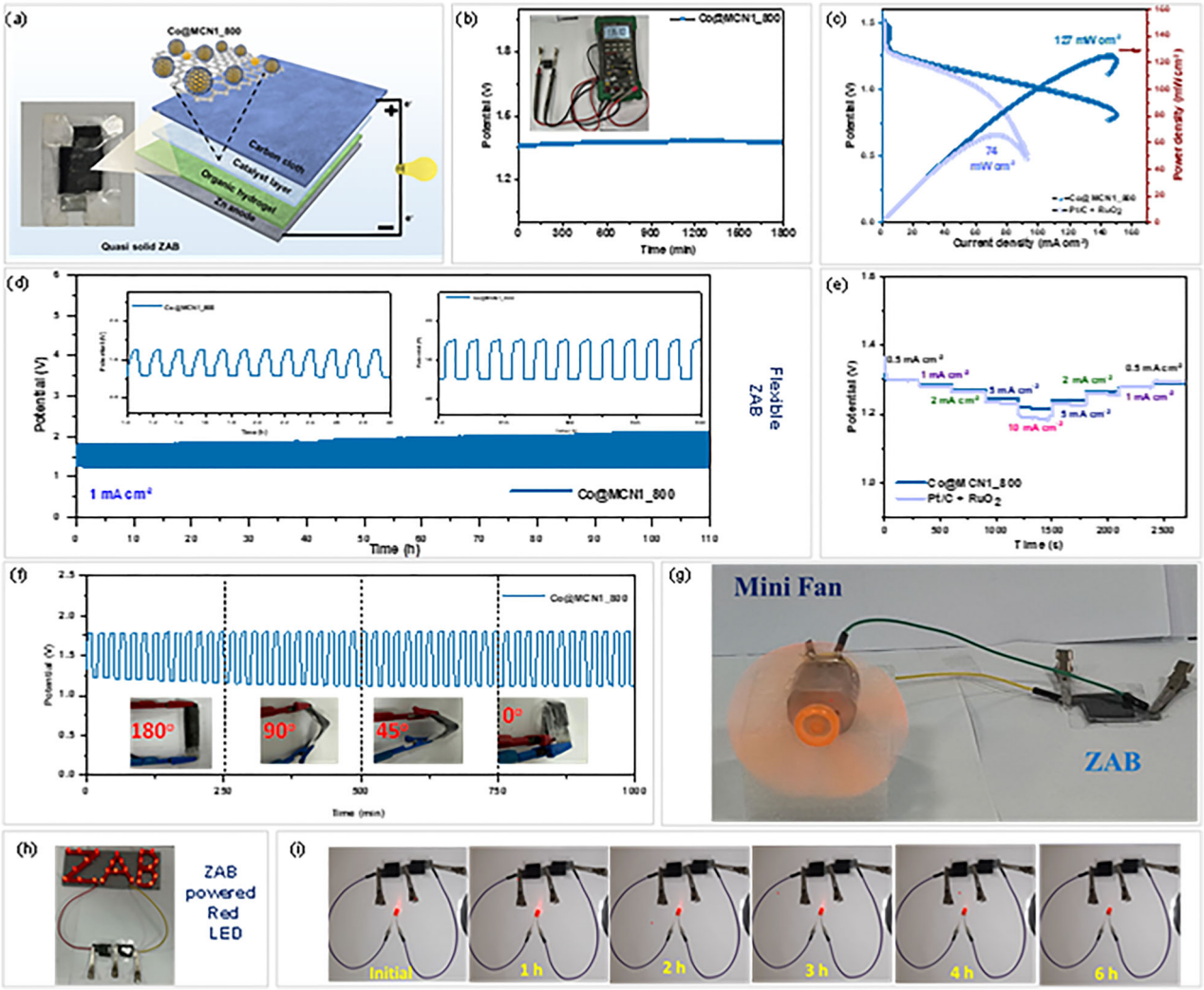

Figure 5. Electrochemical performances of quasi solid-state Zinc-Air battery: a) A solid-state ZAB and schematic diagram of ZAB b) OCV plot of Co@MCN1_800 ZAB; c) Polarization curves and corresponding areal power plots of the Co@MCN1_800 and commercial ($Pt/C+RuO_2$) catalysts; d) Galvanostatic charge discharge cycling stabilities of the ZAB based on Co@MCN1_800 catalyst at 1 $mA.cm^{-2}$ after 5 min of discharge and 5 min of charge (Inset: zoomed data of the charge–discharge cycles at different time interval); e) Rate performance of flexible ZAB at different current densities; f) A charge discharge profile of Co@MCN1_800 based flexible ZAB at 2 $mA.cm^{-2}$ for 10 min of charge and 10 min of discharge (Inset: digital images of flexible ZAB at different bending angles; g) A mini fan was powered by ZAB and h) to light up the "ZAB" LED panel by two ZABs connected in a series; i) Optical images of a light-emitting diode powered up to 6 h.

red LED (≈2.75 V). To our delight, the setup maintained a stable "red LED" at ≈ 2.75 V for 6 h, with the potential decreasing to ≈2.30 V after 6 h, reflecting a voltage drop of ≈0.45 V only. (Figure 5i). Overall, these findings highlight the significant potential of Co@MCN1_800-based cathodes for enabling high-performance, flexible, and rechargeable ZABs suitable for real-world portable and wearable energy applications.

2.4. Theoretical Studies

2.4.1. DFT

To explore the catalytic roles of nitrogen-doped carbon and cobalt centers, we conducted density functional theory (DFT) calculations on six representative active site models. These models include pristine graphene (C(gr)), graphitic nitrogen-doped graphene (N(gr)), pyridinic nitrogen-doped graphene (N(py)), and their cobalt-supported counterparts: Co@C(gr), Co@N(gr), and Co@N(py). **Figure 6a** presents the constant-potential free-energy diagrams for ORR (right-to-left) and OER (left-to-right), computed within a grand-canonical DFT (GC-DFT) framework that incorporates potential-dependent energetics. This constant-potential GC-DFT framework explicitly accounts for electrode potential, providing a more realistic description than conventional fixed-charge DFT. The optimized adsorption structures of key intermediates (*OOH, *O, and *OH) are shown in Figure S20 (Supporting Information), confirming preferential adsorption on carbon atoms rather than nitrogen dopants. To more realistically capture the electrochemical environment and address

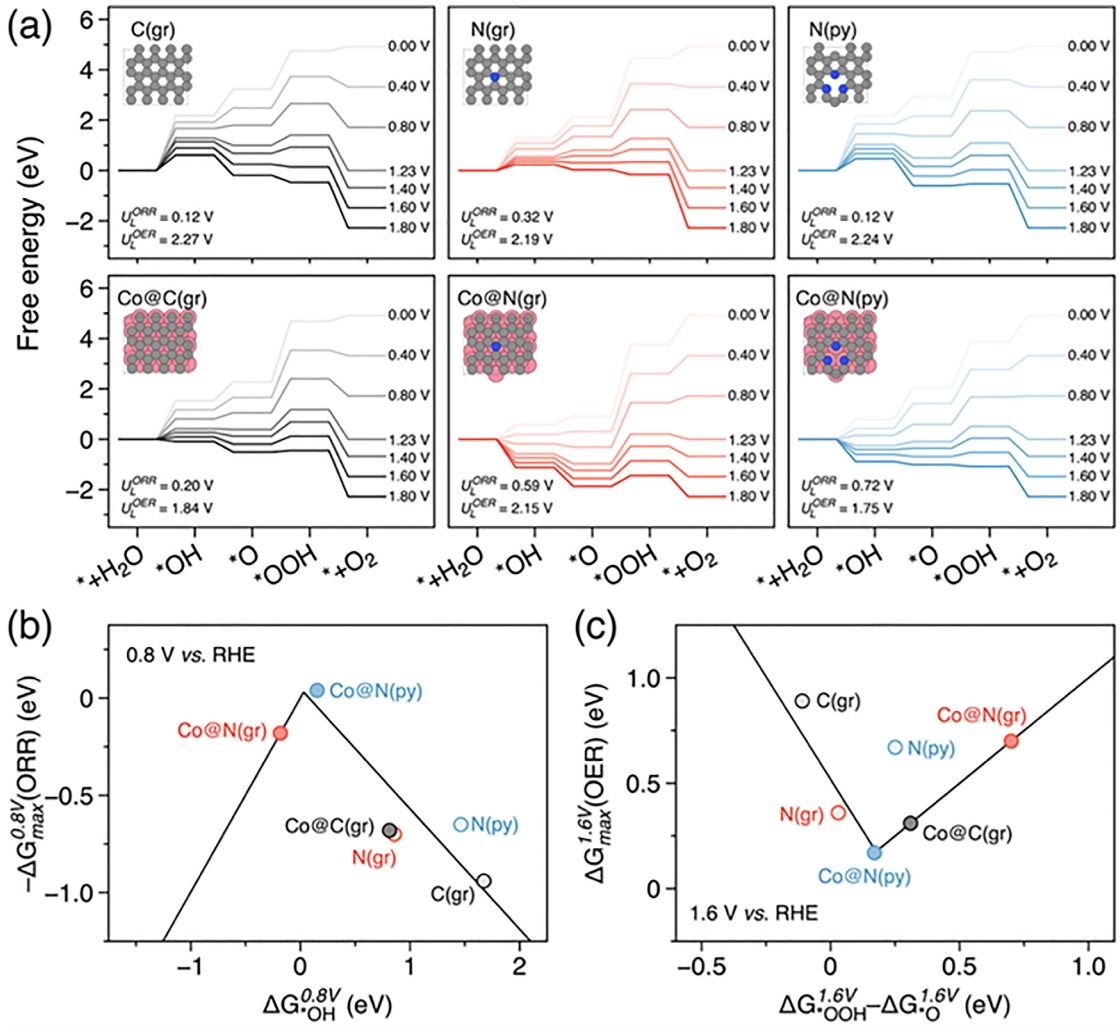

Figure 6. a) Constant-potential free-energy diagrams for oxygen reduction reaction (ORR) and oxygen evolution reaction (OER) on pristine graphene (C(gr)), graphitic N-doped graphene (N(gr)), pyridinic N-doped graphene (N(py)), and cobalt-anchored systems (Co@C(gr), Co@N(gr), Co@N(py)). The reaction coordinate is shown from left to right for OER and from right to left for ORR. The corresponding limiting potentials for ORR (U_L^{ORR}) and OER (U_L^{OER}) are indicated. b) ORR Volcano plot at 0.8 V versus RHE, showing the correlation between the negative maximum reaction free energy ($-\Delta G_{max}$(ORR)) and ΔG_{*OH}. c) OER volcano plot at 1.6 V versus RHE, correlating the maximum reaction energy free energy (ΔG_{max}(OER)) with $\Delta G_{*OOH} - \Delta G_{*O}$.

electrolyte–interface effects, we applied implicit-solvation corrections and fitted the grand potential $\Omega(U)$ to quadratic functions (Figure S21, Supporting Information), evaluated at 0.00, 0.40, 0.80, 1.23, 1.40, 1.60, and 1.80 V versus RHE. The limiting potentials (U_L) were derived from the condition $\Delta G_{max}(U) = 0$ (Figure S22, Supporting Information). In the absence of cobalt centers, both pristine and nitrogen-doped carbons exhibit weak intermediate adsorption and high overpotentials. In contrast, cobalt anchoring markedly strengthens intermediate adsorption and reduces the maximum reaction free-energy (ΔG_{max}) and associated overpotentials. Among the investigated sites, Co@N(py) exhibits the highest activity (U_L^{ORR} = 0.72 V and U_L^{OER} = 1.75 V), placing it closest to the volcano apex for both ORR and OER (Figure 6b,c). Co@N(gr) shows the second-best ORR activity (U_L^{ORR} = 0.60 V) but a high OER overpotential (U_L^{OER} = 2.15 V), whereas Co@C(gr) is favorable for OER (U_L^{OER} = 1.85 V) but less active for ORR (U_L^{ORR} = 0.20 V). To understand the origin of this behavior, we performed a detailed analysis of charge distribution and electronic structure. Bader charge analysis (Figure S23a, Supporting Information) revealed that carbon atoms adjacent to pyridinic nitrogen exhibit a higher positive charge than those near graphitic nitrogen or in pristine graphene. Charge density difference plots (Figure S23b, Supporting Information) confirmed electron transfer from the Co centers to the surrounding carbon layers, with values of 2.05, 2.03, and 2.25e for Co@C(gr), Co@N(gr), and Co@N(py), respectively. Projected density of states (PDOS) analysis showed a negative shift in the p-band center of the carbon atom for Co@N(py) compared to C(gr), which correlates with stronger *OH binding (Figure S24a, Supporting Information). This trend was further supported by the relationship between *OH binding energy and p-band center position across all models (Figure S24b, Supporting Information).

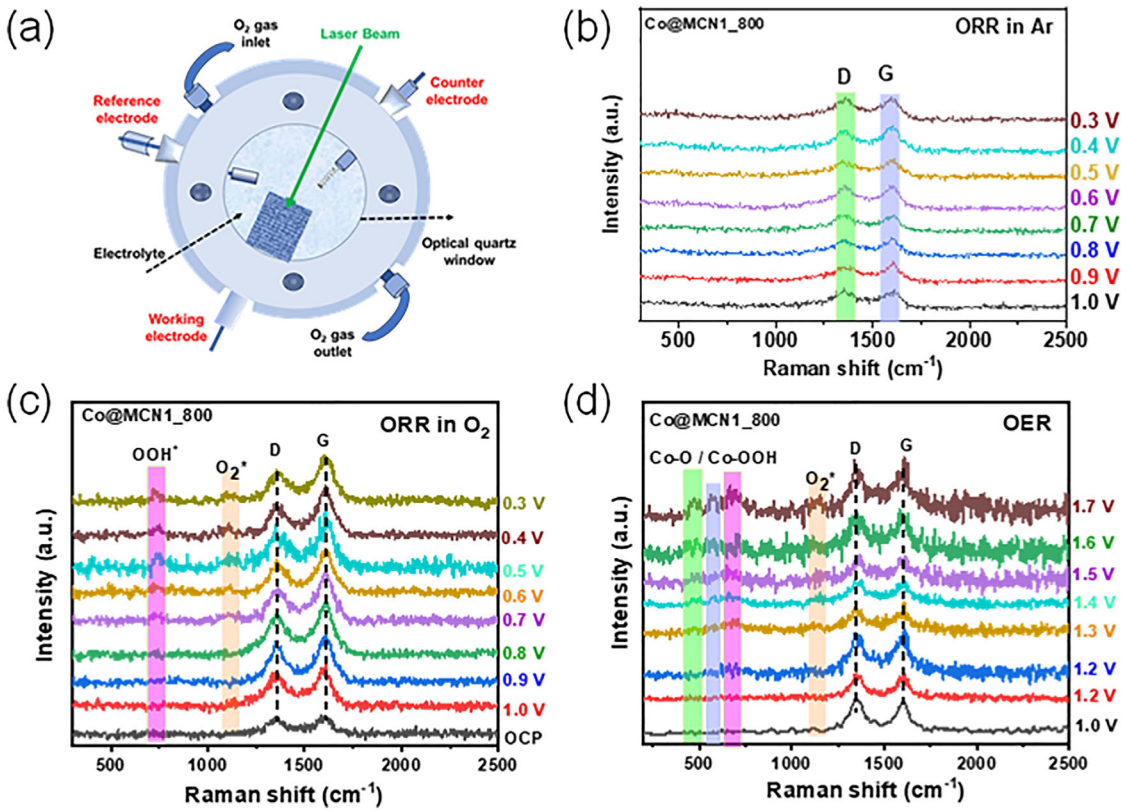

Figure 7. a) In situ Raman cell setup for ORR and OER. In situ Raman spectra of Co@MCN1_800 for ORR in Ar-saturated solution at various potentials. c) In situ Raman spectra in oxygen saturated 0.1 M KOH electrolyte solution at various potential and d) In situ Raman spectra for OER in 1.0 M KOH electrolyte solution at various potential range (1.0 –1.7 V vs RHE).

Overall, Co@N(py) is identified as the most catalytically active site. The active site is attributed to the carbon atom adjacent to pyridinic nitrogen and coordinated with a cobalt center, which enables optimal intermediate adsorption and promotes both ORR and OER with minimal overpotentials.

2.5. Mechanistic Studies via In Situ Raman Spectroscopy

2.5.1. In Situ Raman

The oxygen reduction reaction (ORR) and oxygen evolution reaction (OER) are complex, multi-step processes involving multiple oxygenated intermediates, with their pathways and reactivity highly dependent on the catalyst's surface-active sites and structure. As discussed in the theoretical section, in alkaline media the 4-electron pathway is involved during ORR and OER in alkaline media. Previous RRDE measurements for the Co@MCN1_800 catalyst confirmed its predominant 4-electron pathway. To further elucidate the identities and dynamic behavior of adsorbed intermediates on the Co@N(py) active sites on Co@MCN1_800 catalyst surface during ORR and OER, in situ Raman spectroscopy was systematically conducted in alkaline electrolyte under both Ar- and O_2-saturated conditions, the cell setup for in situ Raman experiment as shown in **Figure** 7a.[61–65] The characteristic D and G bands of the carbon framework were consistently observed, indicating structural stability of the Co@MCN1_800 catalyst throughout the potential range (Figure 7b–d). Notably, in the Ar-saturated environment, no additional peaks emerged as the potential was swept from 1.0 to 0.3 V versus RHE, further confirming the inertness of the carbon matrix in these conditions (Figure 7b). However, when the electrolyte was saturated with O_2 gas, two distinct Raman bands appeared at ≈ 1097 and 728 cm^{-1} as the potential ranged from 0.70 to 0.30 V versus RHE (Figure 7c). These are assigned to the $^*O_2$ and *OOH intermediates, which play crucial roles in the 4-electron ORR pathway. The intensities of these peaks increased with decreasing potential, indicating an accumulation of intermediates followed by their subsequent consumption and a hallmark of a dynamic catalytic process. For OER, applying potentials from 1.0 to 1.7 V versus RHE produced new signals at 473, 574, and 680 cm^{-1}, attributable to the vibrational modes (Eg and Ag) of Co-O and Co-OOH* species respectively, which are vital intermediates for oxygen evolution (Figure 7d). At higher potentials, an emergent peak at 1130 cm^{-1} was detected, indicative of $O_2{}^*$ species, and its intensity correlated with increasing overpotential. The sequential appearance and modulation of these Raman spectra distinctly track the formation and transformation of key intermediates throughout the OER process. Taken together, the in-situ Raman data provide direct spectroscopic evidence for the dynamic participation of $O_2{}^*$, OOH*, Co-O*, and Co-OOH* at the Co@N(py) active sites, substantiating the predominance of the four-electron ORR and OER

mechanisms in Co@MCN1_800 catalyst. These results highlight the role of cobalt centers as principal active sites and confirm that the catalyst maintains high selectivity and activity via well-defined intermediate pathways.

3. Conclusion

In summary, we have developed an *N*-doped graphitic shell–encapsulated cobalt catalyst through a scalable MOF-mediated confined pyrolysis strategy. The optimized Co@MCN1_800 catalyst features gradient N-doped carbon shells with active sites for both the ORR and OER, achieved via controlled pyrolysis of a Co-DABCO-TPA MOF supported on Vulcan carbon. This unique architecture, coupled with electronic modulation, imparts exceptional bifunctional catalytic activity. In alkaline media, Co@MCN1_800 exhibits remarkable ORR performance ($E_{1/2}$ = 0.81 V vs RHE, J_L = 5.3 mA cm^{-2}), comparable to commercial Pt/C, along with competitive OER activity. When implemented in Zn–air batteries, it delivers superior power density and long-term durability. A quasi-solid Zn–air battery (ZAB) employing Co@MCN1_800 maintains a stable open-circuit voltage (OCV) of 1.360 V for up to 10 000 s. Furthermore, the discharge polarization curves demonstrate a peak power density of 127 mW cm^{-2}, significantly outperforming the Pt/C + RuO_2 benchmark catalyst (74 mW cm^{-2}). The theoretical study and in situ Raman study reveal active site for ORR and OER is Co@N(py) where the interface of Co and pyridinic N-atom redistributes the local charge density to optimized adsorption energy for reaction intermediates to facilitate the catalytic reaction. This study presents a rational and scalable design strategy for the development of high-performance, non-precious, monometallic bifunctional electrocatalysts for next-generation energy conversion and storage devices.

Supporting Information

Supporting Information is available from the Wiley Online Library or from the author.

Acknowledgements

M.B. and P.R. contributed equally to this work. SD thanks the University of Bayreuth for generous support and UBT start-up funding. P.R. thanks CSC. R.S.D. acknowledges the BRNS funding agency (58/14/19/2023-BRNS) for research support. GK thanks UGC, New Delhi for fellowship. F.C. thanks and gratefully acknowledge the support from the BayBatt Cell Technology Center, funded by the Deutsche Forschungsgemeinschaft (DFG, German Research Foundation) – INST 91/452-1 LAGG. The project was also funded by the Deutsche Forschungsgemeinschaft (DFG, German Research Foundation) 533115776. F.C. thanks the University of Bayreuth and the Bavarian Center for Battery Technology (BayBatt) for providing start-up funds. B.J.P. acknowledges the support of the Alexander von Humboldt Foundation via a research fellowship. P.K. and A.R. thanks the financial support of the Smart Growth Operational Programme as the XPS measurements were carried out with the equipment purchased by the funding (contract no. POIR.04.02.00-00-D001/20). The financial support of the Strategic Programme Excellence Initiative at Jagiellonian University, used for servicing measurement systems, is also appreciated. A.S. and L.L. are grateful for the beam time provided by the DELTA synchrotron (Dortmund, Germany) and for the support with TEM measurements provided by the Max Planck Institute for Coal Research (Mülheim an der Ruhr, Germany).

Open access funding enabled and organized by Projekt DEAL.

Conflict of Interest

The authors declare no conflict of interest.

Data Availability Statement

The data that support the findings of this study are available from the corresponding author upon reasonable request.

Keywords

bifunctional catalyst, cobalt catalyst, oxygen evolution reaction, oxygen reduction reaction, zinc-air batteries

Received: July 25, 2025
Revised: September 16, 2025
Published online: October 7, 2025

[1] S. Chu, A. Majumdar, *Nature* **2012**, *488*, 294.
[2] Z. P. Cano, D. Banham, S. Ye, A. Hintennach, J. Lu, M. Fowler, Z. Chen, *Nat. Energy* **2018**, *3*, 279.
[3] A. S. Aricò, P. Bruce, B. Scrosati, J.-M. Tarascon, W. van Schalkwijk, *Nat. Mater.* **2005**, *4*, 366.
[4] Y. Li, H. Dai, *Chem. Soc. Rev.* **2014**, *43*, 5257.
[5] J. Fu, Z. P. Cano, M. G. Park, A. Yu, M. Fowler, Z. Chen, *Adv. Mater.* **2017**, *29*, 1604685.
[6] Q. Wang, S. Kaushik, X. Xiao, Q. Xu, *Chem. Soc. Rev.* **2023**, *52*, 6139.
[7] Y. Zhao, D. P. Adiyeri Saseendran, C. Huang, C. A. Triana, W. R. Marks, H. Chen, H. Zhao, G. R. Patzke, *Chem. Rev.* **2023**, *123*, 6257.
[8] L. An, Z. Zhang, J. Feng, F. Lv, Y. Li, R. Wang, M. Lu, R. B. Gupta, P. Xi, S. Zhang, *J. Am. Chem. Soc.* **2018**, *140*, 17624.
[9] D. Yang, H. Tan, X. Rui, Y. Yu, *Electrochem. Energy. Rev.* **2019**, *2*, 395.
[10] J.-N. Liu, C.-X. Zhao, J. Wang, D. Ren, B.-Q. Li, Q. Zhang, *Energy Environ. Sci.* **2022**, *15*, 4542.
[11] J. K. Nørskov, J. Rossmeisl, A. Logadottir, L. Lindqvist, J. R. Kitchin, T. Bligaard, H. Jónsson, *J. Phys. Chem. B* **2004**, *108*, 17886.
[12] Z. Zhao, C. Chen, Z. Liu, J. Huang, M. Wu, H. Liu, Y. Li, Y. Huang, *Adv. Mater.* **2019**, *31*, 1808115.
[13] Q. Sun, X.-H. Li, K.-X. Wang, T.-N. Ye, J.-S. Chen, *Energy Environ. Sci.* **2023**, *16*, 1838.
[14] Q. Shi, C. Zhu, D. Du, Y. Lin, *Chem. Soc. Rev.* **2019**, *48*, 3181.
[15] Y.-F. Guo, X. Liu, S.-J. Yang, P.-F. Wang, Z.-L. Liu, J.-H. Zhang, C.-S. Li, J. Shu, T.-F. Yi, *Chem. Eng. J.* **2024**, *498*, 155537.
[16] G. Kumar, R. S. Dey, *Inorg. Chem.* **2023**, *62*, 13519.
[17] D. Zuo, S. Pradhan, M. Banerjee, N. Rockstroh, S. Bartling, A. I. M. Rabee, X. Tian, A. Skorynina, A. Jaworski, L. Simonelli, J. Rabeah, H. Jiao, M. Beller, S. Das, *Adv. Mater.* **2025**, 2509890.
[18] J. Zhu, G. Li, A. Rokicińska, Z. Wang, P. Kuśtrowski, Z. Lu, S. Das, P. Cool, *Small* **2025**, *21*, 2505306.
[19] P. Ren, T. Zhang, N. Jain, H. Y. V. Ching, A. Jaworski, G. Barcaro, S. Monti, J. Silvestre-Albero, V. Celorrio, L. Chouhan, A. Rokicińska, E. Debroye, P. Kuśtrowski, S. Van Doorslaer, S. Van Aert, S. Bals, S. Das, *J. Am. Chem. Soc.* **2023**, *145*, 16584.
[20] D. Wang, D. Astruc, *Chem. Soc. Rev.* **2017**, *46*, 816.
[21] S. Anantharaj, V. Aravindan, *Adv. Energy Mater.* **2020**, *10*, 1902666.
[22] L. Wen, F. Li, H.-M. Cheng, *Adv. Mater.* **2016**, *28*, 4306.
[23] H. Cui, Z. Zhou, D. Jia, *Mater. Horiz.* **2017**, *4*, 7.
[24] F. K. Kessler, Y. Zheng, D. Schwarz, C. Merschjann, W. Schnick, X. Wang, M. J. Bojdys, *Nat. Rev. Mater.* **2017**, *2*, 17030.
[25] Y. Tu, D. Deng, X. Bao, *J. Energy Chem.* **2016**, *25*, 957.
[26] J.-C. Li, P.-X. Hou, C. Liu, *Small* **2017**, *13*, 1702002.

[27] A. Sarapuu, E. Kibena-Põldsepp, M. Borghei, K. Tammeveski, *J. Mater. Chem. A* **2018**, *6*, 776.
[28] X. Zhu, C. Hu, R. Amal, L. Dai, X. Lu, *Energy Environ. Sci.* **2020**, *13*, 4536.
[29] J. Masa, W. Xia, M. Muhler, W. Schuhmann, *Angew. Chem., Int. Ed.* **2015**, *54*, 10102.
[30] Y. Feng, N. Alonso-Vante, *Phys. Stat. Sol.* **2008**, *245*, 1792.
[31] S. Li, X. Hao, A. Abudula, G. Guan, *J. Mater. Chem. A* **2019**, *7*, 18674.
[32] H. Liu, R. Xiong, S. Ma, R. Wang, Z. Liu, T. Yao, B. Song, *Energy. Adv.* **2025**, *4*, 55.
[33] H. Abba, M. Ladan, H. Musa, I. T. Siraj, A. M. Yamani, A. S. Muhammad, N. M. Kwalam, A.-R. A. Abdul, A. A. Muhammad, S. Habibu, M. Shalauddin, N. Mansir, W. J. Basirun, M. B. Idris, *J. Solid State Electrochem.* **2025**, *29*, 1653.
[34] J. Deng, D. Deng, X. Bao, *Adv. Mater.* **2017**, *29*, 1606967.
[35] X. X. Wang, M. T. Swihart, G. Wu, *Nat. Catal.* **2019**, *2*, 578.
[36] Y. Shao, J.-P. Dodelet, G. Wu, P. Zelenay, *Adv. Mater.* **2019**, *31*, 1807615.
[37] M. Chen, Y. He, J. S. Spendelow, G. Wu, *ACS Energy Lett.* **2019**, *4*, 1619.
[38] Y. Chen, S. Ji, Y. Wang, J. Dong, W. Chen, Z. Li, R. Shen, L. Zheng, Z. Zhuang, D. Wang, Y. Li, *Angew. Chem., Int. Ed.* **2017**, *56*, 6937.
[39] X. X. Wang, V. Prabhakaran, Y. He, Y. Shao, G. Wu, *Adv. Mater.* **2019**, *31*, 1805126.
[40] H.-F. Wang, L. Chen, H. Pang, S. Kaskel, Q. Xu, *Chem. Soc. Rev.* **2020**, *49*, 1414.
[41] C. Gao, F. Lyu, Y. Yin, *Chem. Rev.* **2021**, *121*, 834.
[42] J.-H. Jang, A. A. Jeffery, J. Min, N. Jung, S. J. Yoo, *Nanoscale* **2021**, *13*, 15116.
[43] L. Shen, J. Ying, K. I. Ozoemena, C. Janiak, X.-Y. Yang, *Adv. Funct. Mater.* **2022**, *32*, 2110851.
[44] W. Zhou, J. Zhou, Y. Zhou, J. Lu, K. Zhou, L. Yang, Z. Tang, L. Li, S. Chen, *Chem. Mater.* **2015**, *27*, 2026.
[45] F. Shi, K. Zhu, X. Li, E. Wang, X. Zhu, W. Yang, *J. Energy Chem.* **2021**, *61*, 327.
[46] M.-X. Chen, M. Zhu, M. Zuo, S.-Q. Chu, J. Zhang, Y. Wu, H.-W. Liang, X. Feng, *Angew. Chem., Int. Ed.* **2020**, *59*, 1627.
[47] I. Szewczyk, A. Rokicińska, M. Michalik, J. Chen, A. Jaworski, R. Aleksis, A. J. Pell, N. Hedin, A. Slabon, P. Kuśtrowski, *Chem. Mater.* **2020**, *32*, 7263.
[48] M. C. Biesinger, B. P. Payne, A. P. Grosvenor, L. W. M. Lau, A. R. Gerson, R. S. C. Smart, *Appl. Surf. Sci.* **2011**, *257*, 2717.
[49] D. Eisenberg, P. Prinsen, N. J. Geels, W. Stroek, N. Yan, B. Hua, J.-L. Luo, G. Rothenberg, *RSC Adv.* **2016**, *6*, 80398.
[50] G. Kumar, S. K. Das, C. Nayak, R. S. Dey, *Small* **2024**, *20*, 2307110.
[51] G. Kumar, S. K. Das, T. R. K. Rana, S. Samui, L. Billon, R. S. Dey, *J. Mater. Chem. A* **2024**, *12*, 28085.
[52] Y. Fu, H. Y. Yu, C. Jiang, T. H. Zhang, R. Zhan, X. Li, J. F. Li, J. H. Tian, R. Yang, *Adv. Funct. Mater.* **2018**, *28*, 1705094.
[53] A. Aijaz, J. Masa, C. Rösler, W. Xia, P. Weide, A. J. Botz, R. A. Fischer, W. Schuhmann, M. Muhler, *Angew. Chem., Int. Ed.* **2016**, *55*, 4087.
[54] Y. Li, C. Zhong, J. Liu, X. Zeng, S. Qu, X. Han, Y. Deng, W. Hu, J. Lu, *Adv. Mater.* **2018**, *30*, 1703657.
[55] X. Han, G. He, Y. He, J. Zhang, X. Zheng, L. Li, C. Zhong, W. Hu, Y. Deng, T. Y. Ma, *Adv. Energy Mater.* **2018**, *8*, 1870043.
[56] C. Tang, B. Wang, H. F. Wang, Q. Zhang, *Adv. Mater.* **2017**, *29*, 1703185.
[57] J. Yin, Y. Li, F. Lv, Q. Fan, Y. Q. Zhao, Q. Zhang, W. Wang, F. Cheng, P. Xi, S. Guo, *ACS Nano* **2017**, *11*, 2275.
[58] W. Wan, X. Liu, H. Li, X. Peng, D. Xi, J. Luo, *Appl. Catal., B* **2019**, *240*, 193.
[59] J. Masa, W. Xia, L. Sinev, A. Zhao, Z. Sun, S. Grützke, P. Weide, M. Muhler, W. Schuhmann, *Angew. Chem., Int. Ed.* **2014**, *53*, 8508.
[60] C. Li, X. Han, F. Cheng, Y. Hu, C. Chen, J. Chen, *Nat. Commun.* **2015**, *6*, 7345.
[61] G. Kumar, S. K. Das, E. E. Siddharthan, A. Biswas, S. Bhardwaj, M. Das, R. Thapa, R. S. Dey, *J. Mater. Chem. A* **2023**, *11*, 18740
[62] J. Wei, D. Xia, Y. Wei, X. Zhu, J. Li, L. Gan, *ACS Catal.* **2022**, *12*, 7811.
[63] M. W. Louie, A. T. Bell, *J. Am. Chem. Soc.* **2013**, *135*, 12329.
[64] Z. He, M. Ajmal, M. Zhang, X. Liu, Z. Huang, C. Shi, R. Gao, L. Pan, X. Zhang, J. Zou, *Adv. Sci.* **2023**, *10*, 2304071.
[65] Y. Wang, J. Le, W. Li, J. Wei, P. M. Radjenovic, H. Zhang, X. Zhou, J. Cheng, Z. Tian, J. Li, *Angew. Chem., Int. Ed.* **2019**, *58*, 16062.